

# Nanometer resolution *in situ* structure of SARS-CoV-2 post-fusion spike

**Yun Zhu** (✉ [zhuyun@ibp.ac.cn](mailto:zhuyun@ibp.ac.cn))

Institute of Biophysics, Chinese Academy of Sciences <https://orcid.org/0000-0001-9382-8592>

**Fei Sun**

Institute of Biophysics, Chinese Academy of Sciences <https://orcid.org/0000-0002-0351-5144>

**Xiangxi Wang**

Institute of Biophysics <https://orcid.org/0000-0003-0635-278X>

**Linhua Tai**

<https://orcid.org/0000-0001-8435-9683>

**Guoliang Zhu**

Institute of Biophysics, Chinese Academy of Sciences

**Minnan Yang**

Institute of Biophysics, Chinese Academy of Sciences

**Lei Cao**

CAS Key Laboratory of Infection and Immunity, National Laboratory of Macromolecules, Institute of Biophysics, Chinese Academy of Sciences, Beijing 100101, China.

**Xiaorui Xing**

CAS Key Laboratory of Infection and Immunity, Institute of Biophysics, Chinese Academy of Sciences

**Guoliang Yin**

Institute of Biophysics, Chinese Academy of Sciences

**Chun Chan**

Division of Medicinal Chemistry and Pharmacognosy, College of Pharmacy, The Ohio State University

**Cheng-Feng Qin**

Beijing Institute of Microbiology and Epidemiology

**Rao Zihe**

Shanghai Institute for Advanced Immunochemical Studies, School of Life Science and Technology,  
ShanghaiTech University

---

## Article

**Keywords:** SARS-CoV-2, spike protein, post-fusion state, *in situ* structure, sub-tomogram averaging

**Posted Date:** March 18th, 2021

DOI: <https://doi.org/10.21203/rs.3.rs-303572/v1>

**License:**  This work is licensed under a Creative Commons Attribution 4.0 International License.

[Read Full License](#)

---

## Abstract

The spike protein (S) of severe acute respiratory syndrome coronavirus 2 (SARS-CoV-2) mediates membrane fusion to allow entry of viral genome into host cell. To understand its detailed entry mechanism and develop specific entry inhibitor, the *in situ* structural information of SARS-CoV-2 spikes in different states are urgently important. Here, by using the cryo-electron microscopic tomograms, we observed spikes of inactivated SARS-CoV-2 virions in both pre-fusion and post-fusion states and solved the nanometer resolution structure of *in situ* post-fusion spike. With a more complete model compared to previous reports, the relative spatial position between fusion peptide and transmembrane domain was discovered. Novel oligomerizations of spikes on viral membrane were observed, likely suggesting a new mechanism of fusion pore formation.

## Main Text

In the past two decades, several zoonotic coronavirus (CoV) diseases emerged and posing a devastating threat to global public health and economy, such as severe acute respiratory syndrome (SARS)<sup>1</sup>, Middle East Respiratory Syndrome (MERS)<sup>2</sup> and coronavirus disease 2019 (COVID-19)<sup>3</sup>. As of this writing, COVID-19 has caused more than 120 million confirmed cases and 2.65 million deaths worldwide, with rapidly increasing numbers. This pneumonia epidemic was determined to be caused by a novel coronavirus named severe acute respiratory syndrome coronavirus 2 (SARS-CoV-2). Giving the situation of this pandemic, understanding the architecture and the infection process of SARS-CoV-2 is vital for vaccine development and drug discovery.

During the infection process, one trimeric viral surface protein of SARS-CoV-2 called spike (S) glycoprotein is cleaved by host proteases<sup>4,5</sup> to produce two functional subunits, the N-terminal S1 subunit responsible for receptor recognition and C-terminal S2 subunit responsible for membrane fusion<sup>6</sup>. Both *in vitro* and *in situ* structures of SARS-CoV-2 spike in pre-fusion state as well as their complexes with receptors were studied promptly and extensively using single-particle cryo-electron microscopy (cryo-EM)<sup>7,8</sup>, X-ray crystallography<sup>9–11</sup> and cryo-electron tomography (cryo-ET) and sub-tomogram averaging (cryo-STA)<sup>12,13</sup>, uncovering the different distribution patterns of the conformational states and its native glycosylation.

Both structures of recombinant and *in situ* spike in post-fusion state has been reported<sup>13–16</sup>. However, the *in vitro* study failed to tell how the post-fusion spikes organize on the membrane. Previous *in situ* studies<sup>12,13,15</sup> tended to explore this question but yielded limited information due to poor quality of the density map. Here, we report the *in situ* structure of SARS-CoV-2 post-fusion spike to nanometer resolution (12.6 Å) with high quality of the map, which facilitate better understanding of the viral infection process of SARS-CoV-2 and will be beneficial for the viral entry inhibitor development.

## Results

# Cryo-ET analysis of inactivated SARS-CoV-2 virus

In previous studies, when SARS-CoV-2 virions were inactivated by fixation with formaldehyde, the spikes protruding from the viral surface had two morphologies – a minority in extended and thin structure for post-fusion state, while the majority for pre-fusion state<sup>12</sup>. But when virions were inactivated with nucleic acid modifier β-propiolactone (BPL) at 37°C, it was reported that only thin protrusions for post-fusion spikes were seen on the viral surface<sup>15,17</sup>. In our current study, we propagated SARS-CoV-2 virions in Vero cells and purified viral particles in BSL-3 (biosafety level 3) laboratory. The purified virus was inactivated with BPL prior to following structural characterization in BSL-2 (biosafety level 2) laboratory. To collect enough data to analyze the *in situ* structures of spikes, we acquired a large cryo-ET dataset consisting of 500 tilt-series covering more than 2,000 viruses. In reconstructed tomograms we observed that inactivated SARS-CoV-2 virions exhibit a typical morphology of coronavirus with the diameter range of 80 ~ 120 nm (Fig. 1A). Inside the virion, the ribonucleoprotein complexes were tightly packed with a diameter around 15 nm. The high quality tomograms with deconvolution using Warp<sup>18</sup> enable most spikes to be clearly visualized ready for the subsequent particle picking. These spikes are randomly distributed on viral surface, up to 50 ~ 100 spikes per virion (Fig. S1), much more than ~ 30 spikes per virion observed in previous reports (14). We could observe both post-fusion (Fig. 1A and 1B) and pre-fusion (Fig. S1) spikes as reported previously<sup>15</sup>.

In this study, we mainly focused on the nail shaped spikes on viral membrane, presumably in the post-fusion state, in which S1 subunit has dissociated from S2. It was proved previously that spikes in pre-fusion state do not always protrude straight from the viral membrane, and tilt from vertical axis to viral membrane with a range of 50 degrees could be observed<sup>12</sup>. In contrast, all the post-fusion spikes appear to be perpendicular to the viral surface, suggesting that such conformation should be more stable in the membrane proximal external region (MPER) or transmembrane (TM) region. In most cases of our observation, the post-fusion spikes appear separated alone on the viral membrane (Fig. 1B and Fig. S2A). However, we also noticed that some post-fusion spikes oligomerize like twins in parallel (Fig. 1C) or branches (Fig. 1D and Fig. S2B), suggesting these post-fusion spikes may interact with each other on viral membrane, which has not been reported before and will be discussed later.

After manual picking, statical analysis showed that the numbers of spikes in pre- and post-fusion states account for 61% and 39% of the total number, respectively (Fig. 1E). Such ratio differs substantially with the previous report<sup>15</sup>. Therefore, it is reasonable an optimized inactivation process with BPL could largely avoid the conformational transition from pre-fusion state to post-fusion state. In addition, purification strategies and conditions for plunge freezing are possibly involved in this transition.

## Sub-tomogram averaging of SARS-CoV-2 post-fusion spike

The purified recombinant SARS-CoV-2 S protein could form a stable post-fusion state under specific conditions without target cell, whose structure has been solved to 3.3 Å resolution recently<sup>14</sup>. But it remains unknown whether this *in vitro* structure keeps same on natural viral membrane, and more

importantly, whether the post-fusion state conformation would be further altered along with the formation of fusion pore. Based on our large amount of cryo-ET tomograms, we ought to solve the *in situ* structure of SARS-CoV-2 post-fusion spike (Fig. S3).

Using data-driven template as reference, and performing only local search at the very beginning, we reached a final averaged map of post-fusion spike at 12.6 Å resolution (Fig. 1F, Fig. S3 and Movie S1). The main structural parts of post-fusion spike, including the connector domain, six-helix bundle (6-HB) domain and TM domain, could be clearly distinguished (Fig. 1G). The *in situ* structures of pre-fusion spikes showed the presence of flexible hinges in the stalk region, leading to a large positional and orientational freedom of S1 subunit in the head region<sup>12</sup>. This structural feature could help the pre-fusion spike seek and bind to the ACE2 receptor of the target cell. After the drastic allosteric change of S2 subunit, its heptad repeat 1 (HR1) and heptad repeat 2 (HR2) domains bind to each other to form 6-HB in the post-fusion state. This 6-HB structure is highly thermodynamically stable, and thereby enabling the head region (connector), stalk region (6-HB) and even transmembrane region (TM) visible in the alignment process (Fig. 1G and Fig. S3). Almost all the post-fusion spikes are perpendicular to the viral membrane (Fig. 1H). During the evolution of coronavirus, the S2 subunits keep extremely high conservation in both sequence and structure<sup>11</sup>, which ensures the stable structure of post-fusion spike and the membrane fusion efficiency.

### Structural model of *in situ* post-fusion spike of SARS-CoV-2

The *in situ* structure of post-fusion spike of SARS-CoV-2 has the length of ~210 Å and width of ~87 Å at the ectodomain (Fig. 2A). Its overall architecture resembles the previously reported recombinant post-fusion spike (EMDB entry EMD-22293)<sup>14</sup> with an unusually long (>180 Å) and rigid 6-HB formed by HR1 and HR2 domains (Fig. S4). Using domain assignment from previously determined pre- and post-fusion spike protein, we built the *in situ* structural model of SARS-CoV-2 post-fusion spike, which is more complete with the extension at the connector, FP and TM domains, when compared to previous reports<sup>14</sup> (Fig. 2B and 2C). The connector domain (residues from G700 to R815) between S1 and S2 subunits, together with the linker region between HR1 and HR2 domains (residues from L1034 to G1131), form the head of post-fusion spike. Both the FP domain (residues from S816 to I834) and TM domain (residues from E1195 to V1230) penetrate the lipid bilayer, stabilizing the entire spike on the viral membrane.

Compared to the structure of previously reported recombinant post-fusion spike, the TM domain in micelle could only be visualized after low pass filtering of the map<sup>14</sup>, whereas the TM domain can be easily discerned in our *in situ* map and forms a compact trimeric array beneath HR2 trimer. (Fig. 2A, 2C, Fig. S4A and S4B). Besides, the FP domain, which plays a major role in membrane fusion process and has not been structurally defined before, can be clearly assigned in our map and located surrounding the TM domains (Fig. 2A, 2C, Fig. S4A and S4B). This architecture could explain in sequence why the TM region is located just right after HR2 domain but there is additional long loop between FP and HR1 domains. In addition, at the connector domain, our model extends a bit longer to G700 at the N terminus of S2 subunit and assigns a rigid helix and a flexible linker from A771 to R815 (Fig. 2B and 2C).

Compared to the public available reported *in situ* structures of post-fusion spike of SARS-CoV-2 (EMDB entries EMD-11627 and EMD-30428)<sup>13,15</sup>, our map also exhibits much better quality at the regions of connector, FP and TM domains to disclose more structural details (Fig. S4). More importantly, the hydrophobic region immediately preceding the TM domain (MPER region) was not visible from previous reports. This region plays an important role for S protein trimerization and membrane fusion<sup>19</sup>. With our structure of *in situ* post-fusion spike of SARS-CoV-2, an updated model of how the spike changes its conformation from pre-fusion to post-fusion is proposed (Movie S2), where the TM domains are close to each other and surrounded by FP domains.

## The glycosylation sites in post-fusion state

Viral glycosylation has wide-ranging roles in viral pathogenesis, such as immune evasion by shielding specific epitopes from neutralizing antibodies. Based on the previous study<sup>7</sup>, there are 22 N-linked glycosylation sites in each chain of SARS-CoV-2 S protein, 16 sites situated before FP domain and 6 situated after.

According to the current covered sequence region of our model, there are 9 N-glycosylation sites (N709, N717, N801, N1074, N1098, N1134, N1158, N1173, and N1194) should be observed. However, we only observed 4 N-glycosylation modifications with straightforward densities, N709, N1074, N1158 and N1194 (Fig. 2D). According to previous studies, the glycan types of these observed sites can be divided into two classes. N709 and N1074 sites primarily consist of oligomannose-type modification, whereas N1158 and N1194 contain afucosylated and fucosylated glycans<sup>20</sup>. It is worthy to note that these glycosylation densities were only clear at their root regions, and no heavy glycosylation could be seen unless adjusting the threshold of the map. This possibly suggested that these sugar branches have low homogeneity, or some of these residues were not modified well in host cells. These glycosylation sites are similar to the previously reported *in situ* and *in vitro* structures of post-fusion spikes<sup>13–15</sup>, providing the additional evidence that these post-translational modifications are conserved and widespread in various SARS-CoV-2 strains and should play important roles in viral infections and immune response.

### In situ oligomerization of post-fusion spike

One important process of viral infection of enveloped viruses is the formation of fusion pore between viral and cell membrane, which makes entry of viral genome into host cell possible. This process, as mentioned above, is triggered by the conformational change of S2 subunits from pre-fusion to post-fusion state. Through a “jackknife” transition, HR1 domain inserts the FP into the host cell membrane. Then HR2 domain folds back, resulting FP and TM domains at the same end, which effectively bring viral and cellular membranes in proximity ready for fusion.

During particle picking, we noticed two novel assembly patterns of post-fusion spikes exist on viral membrane, one type of spikes stands parallel to each other (Fig. 1C), and the other type joints at root yet heading out to different directions (Fig. 1D). We plotted back all particles into reconstructed volumes and fitted the final model into plotted back maps, and managed to observe the organizing pattern of these

specific spikes with the side-by-side and branching patterns, respectively (Fig. 3A and 3B). These patterns occupy a small portion of the total post-fusion spikes (Fig. S5).

For the side-by-side pattern, the post-fusion spikes are parallel and closed to each other (< 10 nm for 6-HB domain), whose connector domains are almost close enough to form direct contact. It is worth noting that this novel oligomerization pattern has never been found for the purified S protein or *in situ* prefusion state of spike. Based on this observation, we propose a possible mechanism that the spikes in the side-by-side pattern may interact with each other through flexible HR2 domains in a domain-exchange manner (Fig. 3C). During the folding process of 6-HB from pre-fusion state to post-fusion state, the HR2 domain needs to seek for neighboring HR1 domain for binding. If there are other spikes around, it might be likely that HR2 domain binds to the adjacent HR1 trimer to form a domain-exchange conformation (Fig. 3D). For the branching pattern, spikes stand in branches with jointed root and this oligomerization state may be due to the oligomerization of their fusion peptides (Fig. 3D). These two types of organization patterns of post-fusion spikes may play an important role for the formation of fusion pores (Fig. 3E).

## Discussions

Enveloped viruses use specialized protein machinery to bring viral and cellular membranes in proximity for membrane fusion. Despite extensive studies of protein machineries and their fusion activities, the molecular mechanism in operating viral and cellular membranes to promote their fusion is poorly understood, especially the formation of fusion pore. Some models of membrane fusion leading to virus infection have been proposed and protein machinery oligomerization might facilitate to form fusion pore<sup>21–23</sup>. In our study, we discovered novel *in situ* oligomerization patterns of post-fusion spikes on viral membrane. On this basis, we proposed a novel possible model of SARS-CoV-2 infection (Fig. 3E). After the interaction between S1 subunit and human ACE2 receptor, the S2 subunit is exposed and undergoes the conformational change to insert FP into target cell membrane. At this point, if there are multiple spikes nearby, they could oligomerize in this local region, leading to a more efficient formation of viral fusion pore.

It has been reported previously that the activation and conformational change of SARS-CoV-2 spike protein require two cleavages by the proprotein convertase furin at the S1/S2 site and the transmembrane serine protease 2 (TMPRSS2) at the S2' site<sup>24,25</sup>. The second cleavage site between R815 and S816 (S2' site) could directly expose FP domain of S2 subunit to insert into host membrane (Fig. 2B). In the *in situ* cryo-STA map of post-fusion spike in our study, there are clear densities located inside the membrane surrounding the TM domains, which is modeled to be FP domain in our model (Fig. 2C and Movie S1). According to this model, the FP domain (start with S816) locates far away from the connector domain (end with R815), suggesting that the post-fusion state of spike protein could be only formed after the cleavage of the S2' site.

During SARS-CoV-2 infection process, the HR1 and HR2 domains interact with each other to bring viral and cellular membrane close enough to form fusion pore (Movie S2), which makes 6-HB an important

target for development of viral entry inhibitors. In this study, we found that the HR2 region has much weaker density in comparison with HR1 domain in this *in situ* structure, suggesting a possibility that some portion of spikes may have only trimer HR1 domain waiting for HR2 domain binding. This could represent the intermediated stage during viral infection. As a result, the HR2 derived peptides designed to have a high binding affinity with HR1 trimer could have the chance to target the exposed HR1 domain and then block the 6-HB formation. When comparing our *in situ* model with the crystal structure of SARS-CoV-2 6-HB reported previously by us<sup>5,11</sup>, we could note that the 6-HB region share the same conformation and the HR1 trimer could be exposed outward completely. This suggest that the previous crystal structure can represent the natural conformation of post-fusion spike 6-HB on the membrane. This is another structural evidence to prove our previous inhibitor design, the highly potent pan-coronavirus fusion inhibitor EK1C4 that can inhibit the infection of SARS-CoV-2 and other known human coronaviruses<sup>11</sup>. The similar strategy has also been used to develop inhibitors for other viruses, e.g. HIV-1<sup>26</sup>, LASV<sup>27</sup>, and MERS-CoV<sup>28</sup>.

As a widely used inactivation reagent to manufacture viral vaccines, BPL could not only chemically modify nuclei acids, but also, to some extent, causes effects on viral proteins<sup>29,30</sup>. It has also been reported that BPL treatment could inhibit membrane fusion process of influenza virus via altering structures and functions of viral proteins<sup>31</sup>. However, in the present study, our BPL inactivation and sample preparation procedure could still keep a reasonable ratio of prefusion to post-fusion states, encouraging us to further optimize our inactivation strategy for better vaccine development.

In summary, our present work proposes a more complete model of post-fusion spike of SARS-CoV-2 and discovers its novel oligomerization states on the membrane that could have important function in the viral infection process, providing further structural information for the next development of viral entry inhibitors.

## Methods

### Facility and ethics statements

All experiments with live SARS-CoV-2 viruses were performed in the enhanced biosafety level 3 (P3+) facilities in the Academy of Military Medical Sciences (AMMS), China (Assurance Number: IACUC-DWZX-2020-001). All experiments were carried out in accordance with the Regulations in the Guide for the Ministry of Science and Technology of the People's Republic of China.

### Virus purification and Cryo-ET sample preparation

Vero cells (ATCC, CCL-81) were maintained in Dulbecco's Modified Essential Medium supplemented with 10% fetal bovine serum (FBS) (Biowest) at 37 °C with 5% CO<sub>2</sub>. The strain of BetaCoV/wuhan/AMMS01/2020 was originally isolated from a COVID-19 patient returning from Wuhan, China. The virus was amplified and titrated by standard plaque forming assay on Vero cells, as previously

reported<sup>33,34</sup>. SARS-CoV-2 was cultured in large-scale Vero cells factories at a multiplicity of infection (MOI) of 0.5 at 37°C with 5% CO<sub>2</sub>. To inactivate virus production, β-propiolactone was thoroughly mixed with the supernatant of the infected cells at a ratio of 1:4,000 v/v for 48 hours at 2 to 8 °C. Following clarification of cell debris and ultrafiltration, the inactivated viruses were purified by Ion-exchange Chromatography (IEC) and Size Exclusion Chromatography (SEC), as previously reported<sup>35,36</sup>. Purified virus was mixed 5:1 (virus: gold) with 10 nm protein A-coated gold fiducials (UMC Utrecht). Then 3 µL of the mixture was applied onto a discharged 300 mesh copper grid with a C-flat™ R 2/1 holey carbon support film. Grids were blotted for 3 s in 100% relative humidity for plunge-freezing (Vitrobot, FEI) in liquid ethane.

## Cryo-ET data acquisition

Cryo-grids were loaded into a FEI Titan Krios G2 transmission electron microscope (Thermo Fisher Scientific, USA) operated at 300 kV and images were recorded on a Gatan K2 Summit DDD camera (Gatan Company, USA) equipped with a Gatan Quantum energy filter with a slit width of 20 eV in zero-loss mode in super resolution mode. Nominal magnification was set to be 105,000x, resulted in a calibrated physical pixel size of 1.36 Å on specimen level. Tilt series between -60° to +60° were acquired using dose-symmetric scheme<sup>37</sup> with a 3° angular increment using SerialEM software with in-house script<sup>38</sup>. A total dose of 123 e<sup>-</sup>/ Å<sup>2</sup> per tilt series was distributed evenly among 41 tilts. The defocus range was set between -1.5 µm and -3 µm and 10 frames were saved for each tilt angle.

## Image processing and sub-tomo averaging

The output super resolution movies were first subjected to motion correction with a binning factor of 2 using Warp, resulted in a pixel size of 1.36 Å, picking and masking of fiducial markers was also done using boxnet tools inside Warp. Then all tilt-series stacks were generated using automatic procedures in Warp, alignment of tilt-series and transformation of alignment file formats were done using a wrapped package<sup>39</sup> of automatic tilt-series alignment functions in Dynamo<sup>40</sup> and IMOD<sup>32</sup> packages. Then alignment files were transferred back to Warp to do per-tilt CTF estimation to be ready for further processing. Tomograms were reconstructed in Warp at a binning level of 8 and deconvolved for better visualization of viral spike. All spikes in post-fusion state were manually picked from 500 tomograms using Dynamo packages<sup>40</sup>. With many attempts we found that it is impossible to align the post-fusion spike particles if the shift and rotation parameters searching were not limited to a reasonable range, or in other words, using the traditional global search strategy. This would be presumably due to the interference of viral membrane and the relative low molecule weight of post-fusion spike (less than 200 kDa). Thus during particle picking process, all particles' initial Euler angles (2 out of 3) were determined based on the vector between manually set two points, one in the middle of the spike and one on the membrane where spike anchors, respectively. Then coordinates and orientations of the particles were employed for the extraction of 9404 sub-volumes into cubic sub-volumes of 48 voxels at a pixel spacing of 10.88 Å and the corresponding 3D CTF models, which also consider radiation damage by accumulated electron dose.

Further alignment and reconstruction of post-fusion Ss were all carried out using RELION ver3.0 & 3.1<sup>41,42</sup>. To avoid any model bias, no prior structures or maps from other studies were used as references throughout the whole data processing steps. First, the sub-tomograms were directly averaged without alignment and symmetry applied to generate a data-driven low-resolution template with only manually set Euler angles applied using *relion\_reconstruct*, this process lead to a good reference for subsequent alignment (Fig. S3A). From this stage on, all alignment steps were done using local search using different set of search steps. Then one round of 3D classification applying C3 symmetry with K=1 using data-driven template as reference was performed, with search steps of two out-plane Euler angles limited to  $\pm 18$  degree and third in-plane Euler angle unlimited. Then the aligned coordinates and Euler angles of all particles were employed for the extraction of cubic sub-volumes of 72 voxels at a pixel spacing of 5.44 Å in Warp. Another round of 3D classification with K=1 was performed, and the aligned coordinates and Euler angles of all particles were employed for the extraction of cubic sub-tomograms of 144 voxels at a pixel spacing of 2.72 Å in Warp. To further ensure that all the particles aligned correctly during data processing, we plotted the sub-volumes back into the tomograms using their refined coordinates and Euler angles (Fig. 1H), then removed the obviously misaligned particles, this process resulted in 4553 particles. Also, we noticed that during the alignment and refinement process, all sub-volumes only shifted a little in translation comparing with the manual picked coordinates in the tomogram ( $\sim 1$  nm 3 nm for 3 axis, Fig. S3B), indicating the accuracy of our manual picking process, and the particles matched well with the data-driven reference. For the three Euler angles, the first one (rot) could be easily determined manually so this Euler angle basically remained unchanged during alignment (5.1–7.0 degree), while the second angle (tilt) changed a little more (20.7–14 degree) and the third angle (psi) showed no correlation with the starting value (Fig. S3C), just as one could expect for a picking process as we did. Final round of refinement was done for sub-volumes at binning level of 2, resulted a final map at 12.6 Å resolution, then resulting half-maps were combined and sharpened using an empirically determined B-factor of -100 (Fig. 1F and 1G).

## Model fitting and data analysis

The previously reported post-fusion structure of purified SARS-CoV-2 spike protein (PDB entry: 6XRA & 6LXT)<sup>11,14</sup> were fitted into the map. The extended parts were built manually using COOT<sup>43</sup> with structure of prefusion spike (PDB entry 6VXX) as reference. The final model was refined using phenix.refine<sup>44</sup>. Visualization and model analysis were performed with UCSF Chimera<sup>45</sup> and UCSF ChimeraX<sup>46</sup>. RMSD calculations were performed considering only the C-alpha atoms of the models.

## Data availability

The Electron Microscopy Database (EMD) accession code of post-fusion spike in this study is EMD-31037, and the corresponding atomic coordinates have been deposited in the Worldwide Protein Data Bank with accession code of 7E9T.

## Declarations

## Acknowledgements

We thank Ping Shan, Ruigang Su and Mengyue Lou (F.S. lab) for their assistance in lab management. We thank the Center for Biological Imaging (CBI), Institute of Biophysics, Chinese Academy of Science for our Cryo-EM work and we would be grateful to Boling Zhu, Xiaojun Huang and Gang Ji for their help of Cryo-EM data collection. We are particularly grateful to Alister Burt for help and useful discussions on image processing and useful script development. We are grateful to Daniel Castaño-Díez and Benjamin Himes for their valuable suggestions and discussions on Dynamo and emClarity usages.

This work was equally supported by grants from Strategic Priority Research Program of Chinese Academy of Sciences (XDB37040102 and XDB29010000), Ministry of Science and Technology of China (2017YFA0504700 and 2020YFA0707500) and National Natural Science Foundation of China (31830020).

This work was also supported by grants from National Science Fund for Distinguished Young Scholars (31925026) and the NSFC Innovative Research Group (81921005), the General Program of National Natural Science Foundation of China (32071187), and National Key Research and Development Program of China (2018YFA0900801, 2018YFA0901102 and 2019YFA0904101).

## Author contributions

1. S., Z. R. and X. W. started the project. F. S., Y. Z. and X. W supervised the project. M. Y., L. C., X. X., C. Q. and L. T. performed the experiments. L. T., Y. Z., G. Z., G. Y. and C. C. performed data collection and solved the structure. Y. Z., L. T., G. Z. and G. Y. analyzed the data and wrote the paper with the substantial input from F. S. and X. W.

## Compliance with ethical standards

All authors declare that they have no conflict of interest. All institutional and national guidelines for the care and use of laboratory animals were observed.

## Competing interests

The authors declare no Competing Financial or Non-Financial Interests.

## References

- 1 Ksiazek, T. G. *et al.* A novel coronavirus associated with severe acute respiratory syndrome. *N Engl J Med***348**, 1953-1966, doi:10.1056/NEJMoa030781 (2003).
- 2 Zaki, A. M., van Boheemen, S., Bestebroer, T. M., Osterhaus, A. D. & Fouchier, R. A. Isolation of a novel coronavirus from a man with pneumonia in Saudi Arabia. *N Engl J Med***367**, 1814-1820, doi:10.1056/NEJMoa1211721 (2012).

- 3 Zhu, N. *et al.* A Novel Coronavirus from Patients with Pneumonia in China, 2019. *N Engl J Med***382**, 727-733, doi:10.1056/NEJMoa2001017 (2020).
- 4 Zhou, P. *et al.* A pneumonia outbreak associated with a new coronavirus of probable bat origin. *Nature***579**, 270-273, doi:10.1038/s41586-020-2012-7 (2020).
- 5 Xia, S. *et al.* Fusion mechanism of 2019-nCoV and fusion inhibitors targeting HR1 domain in spike protein. *Cell Mol Immunol*, doi:10.1038/s41423-020-0374-2 (2020).
- 6 Xia, S. *et al.* The role of furin cleavage site in SARS-CoV-2 spike protein-mediated membrane fusion in the presence or absence of trypsin. *Signal Transduct Target Ther***5**, 92, doi:10.1038/s41392-020-0184-0 (2020).
- 7 Walls, A. C. *et al.* Structure, Function, and Antigenicity of the SARS-CoV-2 Spike Glycoprotein. *Cell***181**, 281-292 e286, doi:10.1016/j.cell.2020.02.058 (2020).
- 8 Wrapp, D. *et al.* Cryo-EM structure of the 2019-nCoV spike in the prefusion conformation. *Science***367**, 1260-1263, doi:10.1126/science.abb2507 (2020).
- 9 Shang, J. *et al.* Structural basis of receptor recognition by SARS-CoV-2. *Nature*, doi:10.1038/s41586-020-2179-y (2020).
- 10 Lan, J. *et al.* Structure of the SARS-CoV-2 spike receptor-binding domain bound to the ACE2 receptor. *Nature*, doi:10.1038/s41586-020-2180-5 (2020).
- 11 Xia, S. *et al.* Inhibition of SARS-CoV-2 (previously 2019-nCoV) infection by a highly potent pan-coronavirus fusion inhibitor targeting its spike protein that harbors a high capacity to mediate membrane fusion. *Cell Res***30**, 343-355, doi:10.1038/s41422-020-0305-x (2020).
- 12 Turanova, B. *et al.* In situ structural analysis of SARS-CoV-2 spike reveals flexibility mediated by three hinges. *Science***370**, 203-208, doi:10.1126/science.abd5223 (2020).
- 13 Yao, H. *et al.* Molecular Architecture of the SARS-CoV-2 Virus. *Cell***183**, 730-738 e713, doi:10.1016/j.cell.2020.09.018 (2020).
- 14 Cai, Y. *et al.* Distinct conformational states of SARS-CoV-2 spike protein. *Science***369**, 1586-1592, doi:10.1126/science.abd4251 (2020).
- 15 Liu, C. *et al.* The Architecture of Inactivated SARS-CoV-2 with Postfusion Spikes Revealed by Cryo-EM and Cryo-ET. *Structure***28**, 1218+, doi:10.1016/j.str.2020.10.001 (2020).
- 16 Ke, Z. *et al.* Structures and distributions of SARS-CoV-2 spike proteins on intact virions. *Nature*, doi:10.1038/s41586-020-2665-2 (2020).

- 17 Klein, S. *et al.* SARS-CoV-2 structure and replication characterized by in situ cryo-electron tomography. *Nat Commun***11**, 5885, doi:10.1038/s41467-020-19619-7 (2020).
- 18 Tegunov, D. & Cramer, P. Real-time cryo-electron microscopy data preprocessing with Warp. *Nat Methods***16**, 1146-1152, doi:10.1038/s41592-019-0580-y (2019).
- 19 Schroth-Diez, B. *et al.* The role of the transmembrane and of the intraviral domain of glycoproteins in membrane fusion of enveloped viruses. *Biosci Rep***20**, 571-595, doi:10.1023/a:1010415122234 (2000).
- 20 Watanabe, Y., Allen, J. D., Wrapp, D., McLellan, J. S. & Crispin, M. Site-specific glycan analysis of the SARS-CoV-2 spike. *Science***369**, 330+, doi:10.1126/science.abb9983 (2020).
- 21 Danieli, T., Pelletier, S. L., Henis, Y. I. & White, J. M. Membrane fusion mediated by the influenza virus hemagglutinin requires the concerted action of at least three hemagglutinin trimers. *Journal of Cell Biology***133**, 559-569, doi:DOI 10.1083/jcb.133.3.559 (1996).
- 22 Lee, K. K. Architecture of a nascent viral fusion pore. *Embo Journal***29**, 1299-1311, doi:10.1038/emboj.2010.13 (2010).
- 23 Martens, S. & McMahon, H. T. Mechanisms of membrane fusion: disparate players and common principles. *Nature Reviews Molecular Cell Biology***9**, 543-556, doi:10.1038/nrm2417 (2008).
- 24 Bestle, D. *et al.* TMPRSS2 and furin are both essential for proteolytic activation of SARS-CoV-2 in human airway cells. *Life Sci Alliance***3**, doi:10.26508/lsa.202000786 (2020).
- 25 Brooke, G. N. & Prischi, F. Structural and functional modelling of SARS-CoV-2 entry in animal models. *Scientific reports***10**, 15917, doi:10.1038/s41598-020-72528-z (2020).
- 26 Zhu, Y. *et al.* Rational improvement of gp41-targeting HIV-1 fusion inhibitors: an innovatively designed Ile-Asp-Leu tail with alternative conformations. *Sci Rep***6**, 31983, doi:10.1038/srep31983 (2016).
- 27 Zhang, X. *et al.* Crystal Structure of Refolding Fusion Core of Lassa Virus GP2 and Design of Lassa Virus Fusion Inhibitors. *Front Microbiol***10**, 1829, doi:10.3389/fmicb.2019.01829 (2019).
- 28 Lu, L. *et al.* Structure-based discovery of Middle East respiratory syndrome coronavirus fusion inhibitor. *Nat Commun***5**, 3067, doi:10.1038/ncomms4067 (2014).
- 29 Uittenbogaard, J. P., Zomer, B., Hoogerhout, P. & Metz, B. Reactions of beta-propiolactone with nucleobase analogues, nucleosides, and peptides: implications for the inactivation of viruses. *J Biol Chem***286**, 36198-36214, doi:10.1074/jbc.M111.279232 (2011).
- 30 Taubman, M. A. & Atassi, M. Z. Reaction of beta-propiolactone with amino acids and its specificity for methionine. *Biochem J***106**, 829-834, doi:10.1042/bj1060829 (1968).

- 31 Bonnafous, P. *et al.* Treatment of influenza virus with beta-propiolactone alters viral membrane fusion. *Biochim Biophys Acta* **1838**, 355-363, doi:10.1016/j.bbamem.2013.09.021 (2014).
- 32 Kremer, J. R., Mastronarde, D. N. & McIntosh, J. R. Computer visualization of three-dimensional image data using IMOD. *J Struct Biol* **116**, 71-76, doi:10.1006/jsbi.1996.0013 (1996).
- 33 Yao, H. *et al.* Rational development of a human antibody cocktail that deploys multiple functions to confer Pan-SARS-CoVs protection. *Cell Res* **31**, 25-36, doi:10.1038/s41422-020-00444-y (2021).
- 34 Wang, N. *et al.* Structure-based development of human antibody cocktails against SARS-CoV-2. *Cell Res* **31**, 101-103, doi:10.1038/s41422-020-00446-w (2021).
- 35 Dong, H. *et al.* Structural and molecular basis for foot-and-mouth disease virus neutralization by two potent protective antibodies. 2020.2012.2031.424923, doi:10.1101/2020.12.31.424923 %J bioRxiv (2021).
- 36 Wang, N. *et al.* Architecture of African swine fever virus and implications for viral assembly. *Science* **366**, 640-644, doi:10.1126/science.aaz1439 (2019).
- 37 Hagen, W. J. H., Wan, W. & Briggs, J. A. G. Implementation of a cryo-electron tomography tilt-scheme optimized for high resolution subtomogram averaging. *J Struct Biol* **197**, 191-198, doi:10.1016/j.jsb.2016.06.007 (2017).
- 38 Mastronarde, D. N. Automated electron microscope tomography using robust prediction of specimen movements. *J Struct Biol* **152**, 36-51 (2005).
- 39 Burt, A., Gaifas, L., Dendooven, T. & Gutsche, I. Tools enabling flexible approaches to high-resolution subtomogram averaging. doi:10.1101/2021.01.31.428990 (2021).
- 40 Castano-Diez, D., Kudryashev, M., Arheit, M. & Stahlberg, H. Dynamo: A flexible, user-friendly development tool for subtomogram averaging of cryo-EM data in high-performance computing environments. *J Struct Biol* **178**, 139-151, doi:10.1016/j.jsb.2011.12.017 (2012).
- 41 Scheres, S. H. W. RELION: Implementation of a Bayesian approach to cryo-EM structure determination. *J Struct Biol* **180**, 519-530, doi:10.1016/j.jsb.2012.09.006 (2012).
- 42 Kimanius, D., Forsberg, B. O., Scheres, S. H. & Lindahl, E. Accelerated cryo-EM structure determination with parallelisation using GPUs in RELION-2. *Elife* **5**, e18722 (2016).
- 43 Emsley, P., Lohkamp, B., Scott, W. G. & Cowtan, K. Features and development of Coot. *Acta Crystallogr D Biol Crystallogr* **66**, 486-501, doi:10.1107/S0907444910007493 (2010).
- 44 Afonine, P. V. *et al.* Towards automated crystallographic structure refinement with phenix.refine. *Acta Crystallogr D Biol Crystallogr* **68**, 352-367, doi:10.1107/S0907444912001308 (2012).

45 Pettersen, E. F. et al. UCSF Chimera—a visualization system for exploratory research and analysis. *J Comput Chem* **25**, 1605-1612, doi:10.1002/jcc.20084 (2004).

46 Pettersen, E. F. et al. UCSF ChimeraX: Structure visualization for researchers, educators, and developers. *Protein Science*, doi:10.1002/pro.3943 (2020).

## Figures

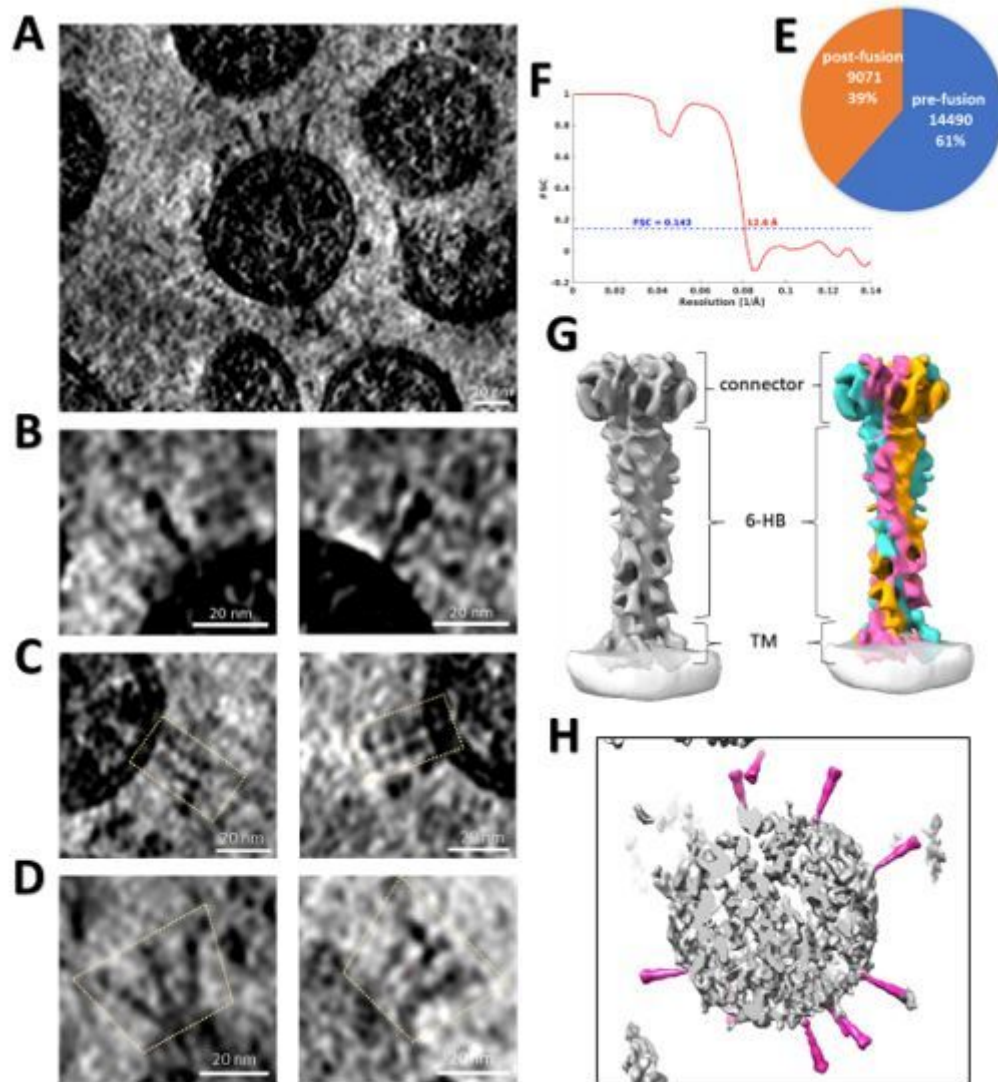
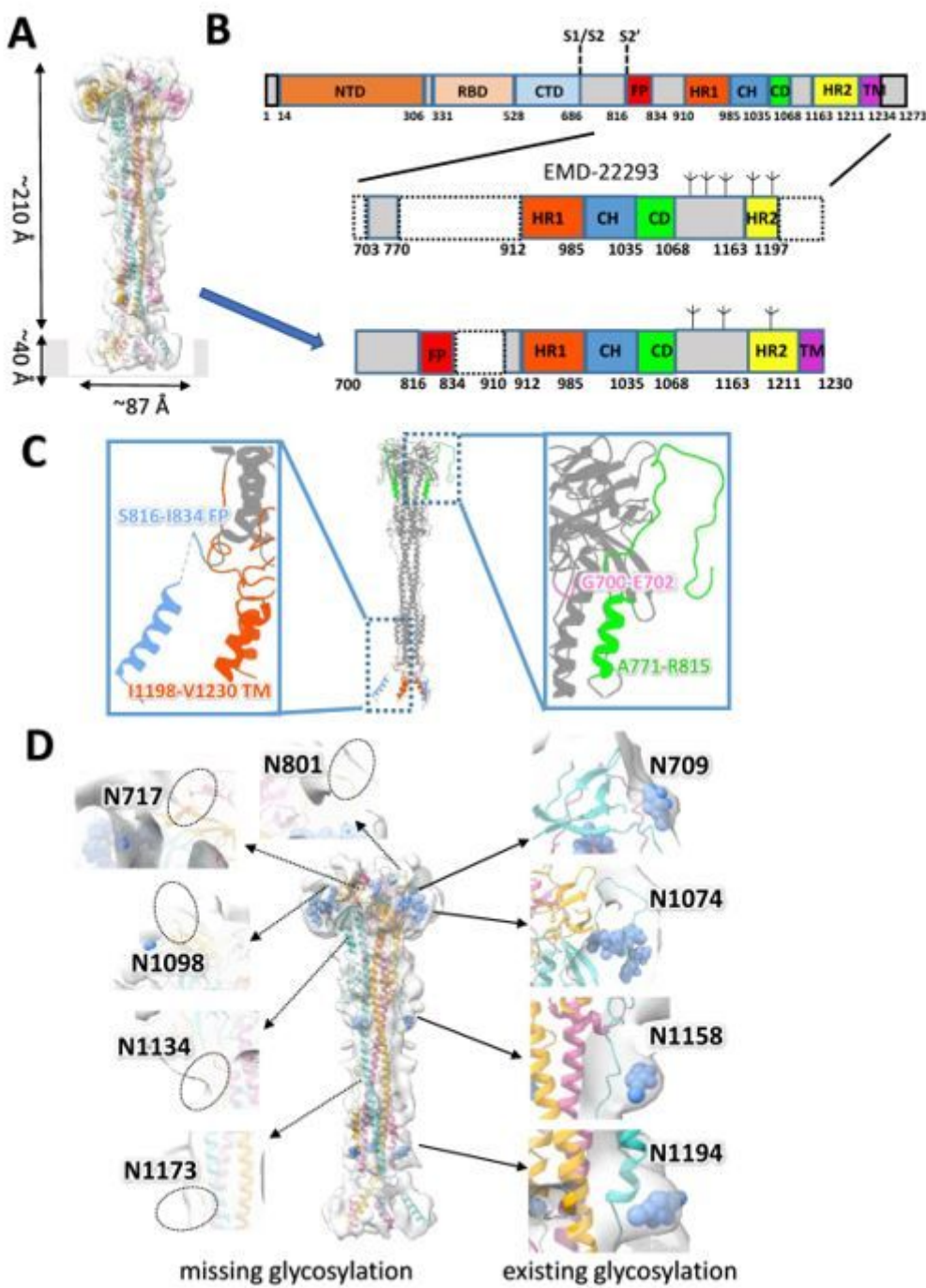


Figure 1

Cryo-electron tomography and sub-tomogram averaging of inactivated SARS-CoV-2 virions, displaying spikes in post-fusion state. (A) Slices through tomographic reconstructions of BPL-inactivated SARS-CoV-2 virions. Scale bar 20 nm. (B) Same as (A) highlighting spikes on the viral membranes in post-fusion states. (C) Same as (B) highlighting twin spikes close to each other. (D) Same as (B) highlighting branch spikes with roots close to each other on the membrane. All tomograms were deconvolved using Warp 18 and shown using IMOD 32. (E) Statistic of manually picked spike particles, 9071 in post-fusion state,

14490 in pre-fusion state. (F) Gold standard FSC of final map of post-fusion spike, showing resolution of 12.6 Å. (G) Full map of post-fusion spike with membrane region (light gray) attached and different domains labeled. The map is colored by dark gray (left) or by three different chains (right). (H) Plotting back sub-tomogram averaged maps (pink) onto the tomogram of a single virion (gray).



**Figure 2**

In situ structure of SARS-CoV-2 post-fusion spike. (A) Geometry of post-fusion spike on the membrane. (B) Domain arrangement of full-length spike protein, and the modelled parts of our structure and the published result (EMD-22293). The two potential cleavage sites are indicated. (C) Extended completion (colored and labeled) of our model compared to the published result (EMD-22293). The overlapping parts

are shown in grey. (D) The observed glycosylation sites in our model are shown in cornflower blue, while the unobserved glycosylation sites marked by dotted circles.

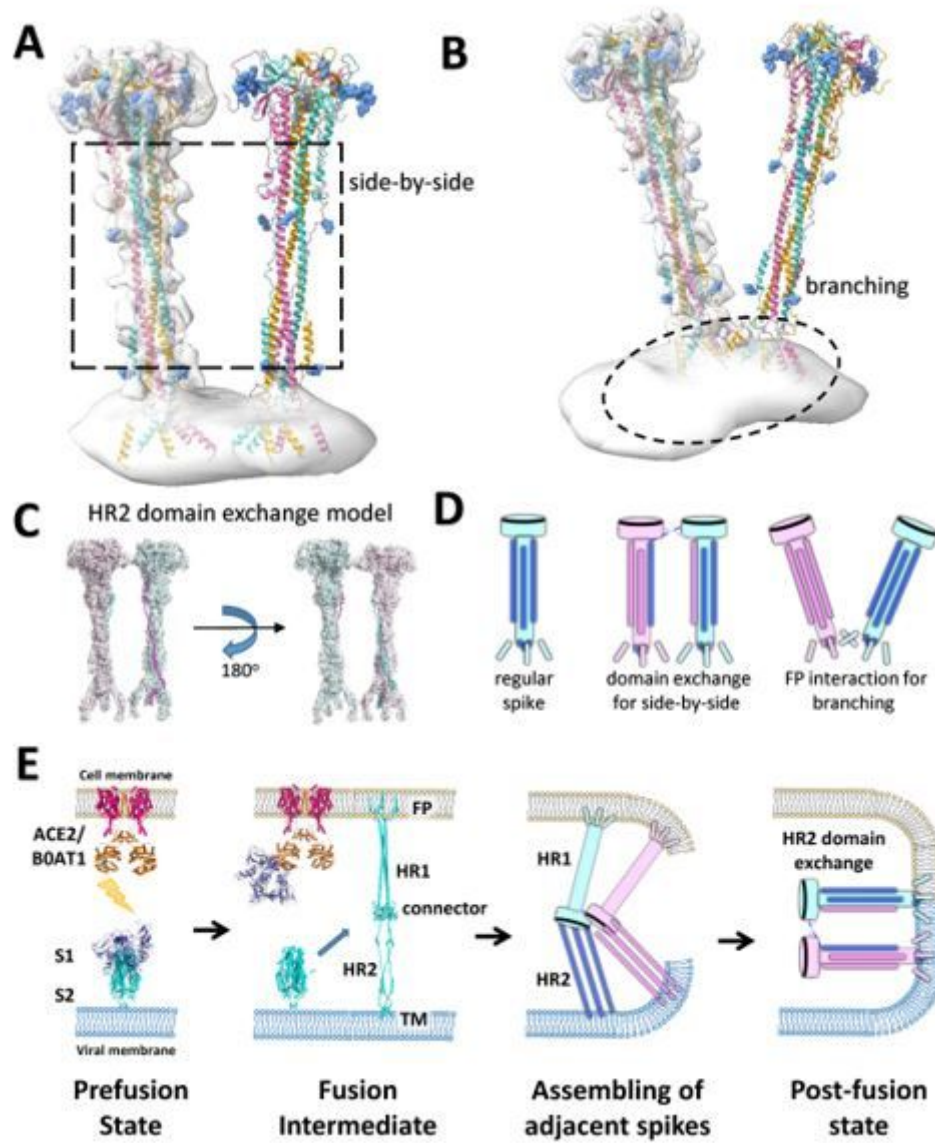


**Figure 3**

Oligomerization arrangement of in situ SARS-CoV-2 post-fusion spikes. (A) Side-by-side post-fusion spikes are shown on membrane with three chains of each spike colored in orange, light sea green and hot pink. The glycosylation sites are all colored by cornflower blue. (B) Post-fusion spikes of branch pattern are shown on membrane with three chains of each spike colored by orange, light sea green and hot pink. The glycosylation sites are all colored by cornflower blue. (C) Possible model of HR2 domain exchange in side-by-side oligomerization state. Two spikes were colored in hot pink and cyan, respectively. (D) Models of in situ post-fusion spikes in regular state, side-by-side state with domain exchange, and branching state with FP interaction. (E) A novel scheme of SARS-CoV-2 spikes transit from prefusion to post-fusion during viral infection and fusion pore formation, where side-by-side spikes are involved.

# Supplementary Files

This is a list of supplementary files associated with this preprint. Click to download.

- [PostFusionMovieS2.mp4](#)
- [PostFusionMovieS1.mp4](#)
- [D1300021032valreportfullP1.pdf](#)